Experimental and numerical study on influence of impact mass and velocity on failure mode of RC columns under lateral impact

Jing-Ming Sun, Hui Chen [*], Fan Yi, Ya-Bo Ding, Yun Zhou, Qing-Feng He, Wang-Xi Zhang, Wei-Jian Yi [*]

College of Civil Engineering, Hunan Provincial Key Lab on Damage Diagnosis for Engineering Structures, Hunan University, Changsha 410082, China

ABSTRACT

Reinforced concrete (RC) structures may encounter impact loads during service life, such as vehicle collisions, ship strikes, and explosions. Limited existing impact tests on RC columns and piers have yet to fully reveal the column impact performance and its relationship with structural or load parameters. To explore the effects of impact mass and velocity, which determine the impact energy, on the impact performance of RC columns, pendulum impact tests on nine RC columns were performed utilizing a specially designed loading setup. The test variables included the impact mass and velocity of the pendulum, as well as the slenderness ratio and stirrup ratio of the columns. During the tests, the impact force and velocity of the pendulum, as well as the axial force, displacement, and acceleration of the columns, were measured. Additionally, the damage evolution of each specimen was recorded using a high-speed camera. One-side shear failure, two-side shear failure near the impact point, and shear failure at the column bottom end were observed during the tests. The results indicated that, under similar impact energy, as the impact velocity increased, the specimens with the low stirrup ratio transitioned from one-side shear failure to two-side shear failure. An enhancement in the impact resistance of the columns was observed when the stirrup ratio was increased, or the slenderness ratio decreased. For the enhanced columns, shear failure was avoided at lower impact velocities; however, at the maximum impact velocity, end shear failure or one-side shear failure yet occurred. Additionally, a parametric analysis using LS-DYNA finite element software further clarified the effects of impact velocity and mass on the dynamic response and failure mode of RC columns.

1. Introduction

The study of impact resistance in concrete structures remains a topic of enduring significance. Reinforced concrete (RC) columns, integral in supporting vertical loads, are particularly vulnerable under extreme impact loading conditions such as vehicle [1–4] and ship [5–7] collisions, as well as explosions [8,9]. The failure of columns can lead to catastrophic structural collapse. Consequently, it is imperative to delve into further experimental and analytical investigations to refine methodologies for the resistance design and performance assessment of RC columns subjected to lateral impact.

Considerable research efforts have been dedicated to comprehending the impact behavior of RC beams [10–19], revealing the substantial influence of varied impact velocities and structural parameters on beam failure modes. A transition in failure modes from bending to shear in RC beams was prevailingly reported when impact velocities were increased

[13,14,16,19], in which specimens with high aspect ratio particularly prone to such changes [17]. Additionally, the damage evolution of RC beams under impact was also investigated [18], showing severe diagonal cracks appeared and expanded within milliseconds, which might lead to shear failure.

Due to differing boundary constraints and internal force states, the impact resistance of RC columns differs from that of beams. However, the number of impact tests on columns is limited, and the application of boundary conditions, particularly the axial force, needs further optimization. Tests by Liu et al. [20] on circular columns revealed that the decrease in the height-to-diameter ratio and the increase in impact energy shift the failure mode from bending to shear. The impact position also demonstrated the capability to alter the failure mode of RC columns [21]. Liu et al. [20] and Gurbuz et al. [21] applied the axial force using disc springs and hydraulic jack, respectively, these methods did not account for the inertia effect induced by the vertical vibration of the
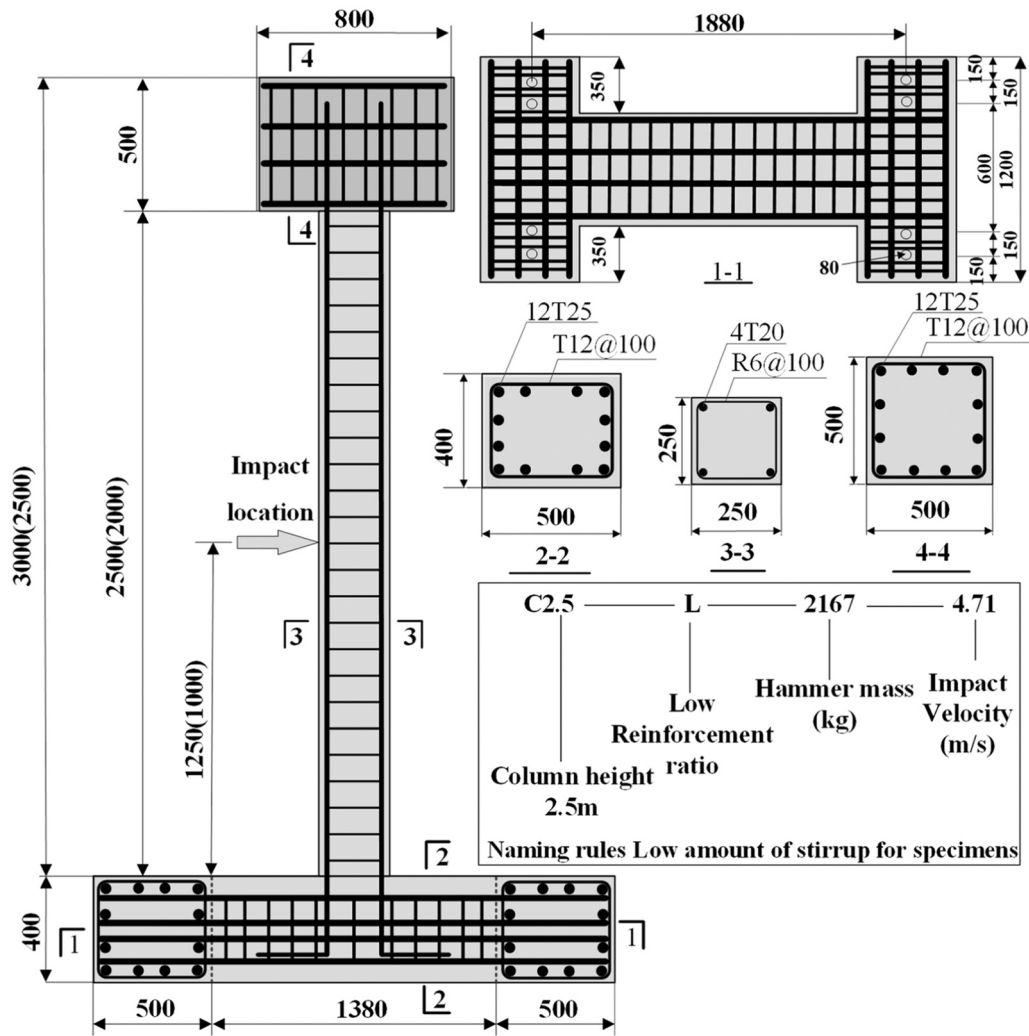
Fig. 1. Reinforcement scheme and geometric dimension of specimens (unit: mm).

superstructure above columns. Sun et al. [22] applied a loading setup specifically designed for pendulum impact tests on columns, allowing for a more precise simulation of the superstructure's influence on column impact performance. The test results [22] showcased notable fluctuations in axial forces during column impact, suggesting a potential impact on the horizontal dynamic response of RC columns.

Horizontal impact and drop weight tests have become key tools for studying impact responses of vertical RC components, particularly for analyzing the dynamic responses of bridge piers subjected to collisions with heavy trucks. These tests encompass a range of impact locations, typically extending from the base to the mid-section of piers [1,20–27]. Through horizontal impact or pendulum tests, researchers have extensively investigated multiple key factors influencing the impact response of RC columns, including axial load ratio [20,22], impact velocity and mass [1,20–24], boundary conditions [1], reinforcement with fiber materials [25,26], and the structural performance of precast segments [27]. Further, numerical simulations using finite element methods have provided detailed analyses of impact mass, velocity, and related structural design parameters [23,28,29]. On the other hand, the introduction of real vehicle models has expanded the focus beyond just the impacted columns to include interactions between vehicles and bridge piers during collisions [30], as well as energy distribution and absorption [3].

Based on the literature review, existing studies typically use either impact mass [24] or initial velocity [1,22,23,25] as the sole input parameters to investigate their effects on the impact response of reinforced

concrete components. Only a few studies have considered the combination of impact mass and velocity [21,29], but the differences in kinetic energy in these studies are usually significant. In contrast, within a performance-based design framework, kinetic energy is a crucial variable for calculating maximum displacement. Indeed, for components subjected to the same kinetic energy or momentum, different combinations of mass and velocity can lead to varied dynamic responses. This indicates that considering the comprehensive effects of kinetic energy is particularly crucial when assessing the impact performance of reinforced concrete components. The impact performance of RC columns is closely related to their failure modes. Understanding their failure mode transition rules is fundamental to developing impact resistance design and damage assessment methods. Variations in structural and load parameters could lead to different failure modes in RC columns. One of the main load parameters is the impact energy, which is determined by the impact mass and velocity. However, existing studies on the impact mass and velocity mainly focus on RC beams. Beam impact tests [19,31] revealed the substantial influence of both mass and velocity on failure modes, even when the impact energy remains unchanged [10]. Currently, a systematic exploration into how impact mass and velocity affect the impact performance and failure modes of RC columns is lacking.

In this study, pendulum impact tests were performed on nine RC columns to investigate the impact of mass and velocity on the structural behavior and failure modes. These tests involved specimens with

Table 1
Design details of each column specimen.

Group Number	Specimen No.	f_{cu} (MPa)	Pendulum mass (kg)	h (m)	λ	Impact velocity (m/s)	Impact energy (kJ)	Axial compression load (kN)
C2.5-L	C2.5-L-2167-4.71	35.9	2167	2.5	10	4.71	24.04	351.9
	C2.5-L-1917-5.21	35.1	1917	2.5	10	5.21	26.02	349.1
	C2.5-L-1667-5.71	37.1	1667	2.5	10	5.71	27.18	347.9
C2.5-H	C2.5-H-2167-4.71	34.8	2167	2.5	10	4.71	24.04	351.2
	C2.5-H-1917-5.21	38.5	1917	2.5	10	5.21	26.02	350.5
	C2.5-H-1667-5.71	33.4	1667	2.5	10	5.71	27.18	347.6
C2-L	C2-L-2167-4.71	34.8	2167	2.0	8	4.71	24.04	348.6
	C2-L-1667-5.71	37.8	1667	2.0	8	5.71	27.18	350.3
	C2-L-1417-6.21	34.5	1417	2.0	8	6.21	27.32	349.2

varying stirrup ratios and heights. Additionally, finite element models were developed for parametric analysis using the LS-DYNA software. Analysis and discussions were centered on the dynamic response and failure modes of RC columns, synthesizing insights from both experimental and numerical findings. This study contributes to a more profound comprehension of the impact failure mechanisms in RC columns, providing valuable insights for the structural design and damage assessment of RC columns under impact loads.

2. Experimental programs

2.1. Specimen design

Engineering accident report [32] indicates that RC bridge columns ranging from 731 to 914 mm in cross-sectional size suffered severe damage due to truck impacts. In this study, prototype columns were designed with a square cross-section measuring 750 mm on each side, falling within the specified range. Column heights of 7.5 m and 6.0 m were selected to investigate the effect of the slenderness on the column impact performance. To accommodate the pendulum testing apparatus, a 1:3 scale reduction from the prototype columns was implemented. Consequently, the test specimens were designed with a side length of 250 mm and heights of 2500 mm and 2000 mm. On the other hand, statistics [32] indicate that the mass of heavy trucks ranges from 14,880 to 62,600 kg, with velocity variations of 11.11 to 27.78 m/s, corresponding to energy ranges of 918 to 24,155 kJ. The test design aimed to explore influences of different combinations of impact mass and velocity on the failure modes and dynamic responses of RC columns when the impact energy remained relatively consistent. The pendulum's mass and the impact velocity were adjusted to range from 1417 to 2167 kg and 4.71 to 6.21 m/s, respectively, with the impact energy variation between 24.0 kJ and 27.3 kJ (within a variation of less than 14 %). The impact energy range in this test, calculated based on similarity theory [33], approximately corresponds to the energy range of 5840 to 6604 kJ in practical engineering accidents.

The test involved 9 RC column specimens, as shown in Fig. 1 and Table 1. The test variables mainly comprised the mass and impact velocity of the pendulum, as well as the stirrup ratio and height (i.e., slenderness ratio) of the columns. The designed axial compression ratio (= N/f_cA, where N is the axial force, A is the cross-sectional area of columns, and f_c is the axial compressive strength of concrete) for the specimens was 0.24. The specimens had a square cross-section with a side length of 250 mm and a concrete cover thickness of 25 mm. The column heights were 2500 mm and 2000 mm, corresponding to slenderness ratios λ (= h/b, where h represents the column height, and b represents the cross-sectional dimension) of 10.0 and 8.0, respectively. The foundation beam had an H-shaped plan with a height of 400 mm, and the column cap had dimensions of 500 mm × 500 mm× 800 mm.

The longitudinal reinforcement and stirrups of the columns were made of ribbed steel bars with a diameter of 20 mm and smooth round steel bars with a diameter of 6 mm, respectively. The longitudinal reinforcement ratio was 2.01 %, and the stirrup spacing was set at
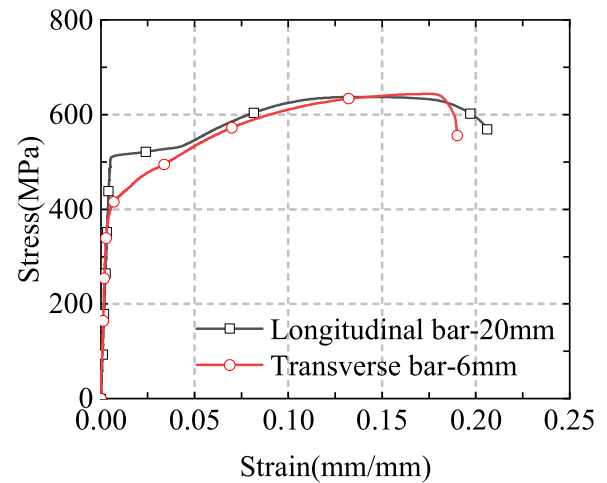

Fig. 2. Stress-strain relationship of reinforcement material as measured.

100 mm and 50 mm, corresponding to stirrup ratios of 0.23 % and 0.46 %, respectively. The longitudinal and stirrup reinforcements of the foundation beam and column cap were made of ribbed steel bars with diameters of 25 mm and 12 mm, respectively.

The naming rules of specimens in Table 1 is explained as follows: Column Height-Stirrup Ratio-Pendulum Mass-Impact Velocity, where L denotes the low stirrup ratio (0.23 %) and H denotes the high stirrup ratio (0.46 %). For example, specimen C2.5-L-2167–4.71 refers to a specimen with a height of 2.5 m, a stirrup ratio of 0.23 %, a pendulum mass of 2167 kg, and an impact velocity of 4.71 m/s. Accordingly, these specimens were divided into three groups based on their height and stirrup ratio: Group C2.5-L (columns with height of 2.5 m and low stirrup ratio), Group C2.5-H (columns with height of 2.5 m and high stirrup ratio), and Group C2-L (columns with height of 2.0 m and low stirrup ratio).

2.2. Materials properties

Measured stress-strain curves for the longitudinal and stirrup reinforcements of the columns are shown in Fig. 2. The 20 mm longitudinal rebars exhibited a yield and ultimate strength of 474 and 638 MPa, respectively, with an elongation rate of 20 %. The yield strength and ultimate strength of the 6 mm stirrups were 409 and 650 MPa, respectively, with an elongation rate of 19 %. Three concrete cubes with a side length of 150 mm were prepared for each specimen. The cubes were cast on the same day as the RC columns and cured under identical conditions. The measured cubic concrete compressive strength f_{cu} on the day of the impact test is listed in Table 1.

2.3. Test setup and instrumentation

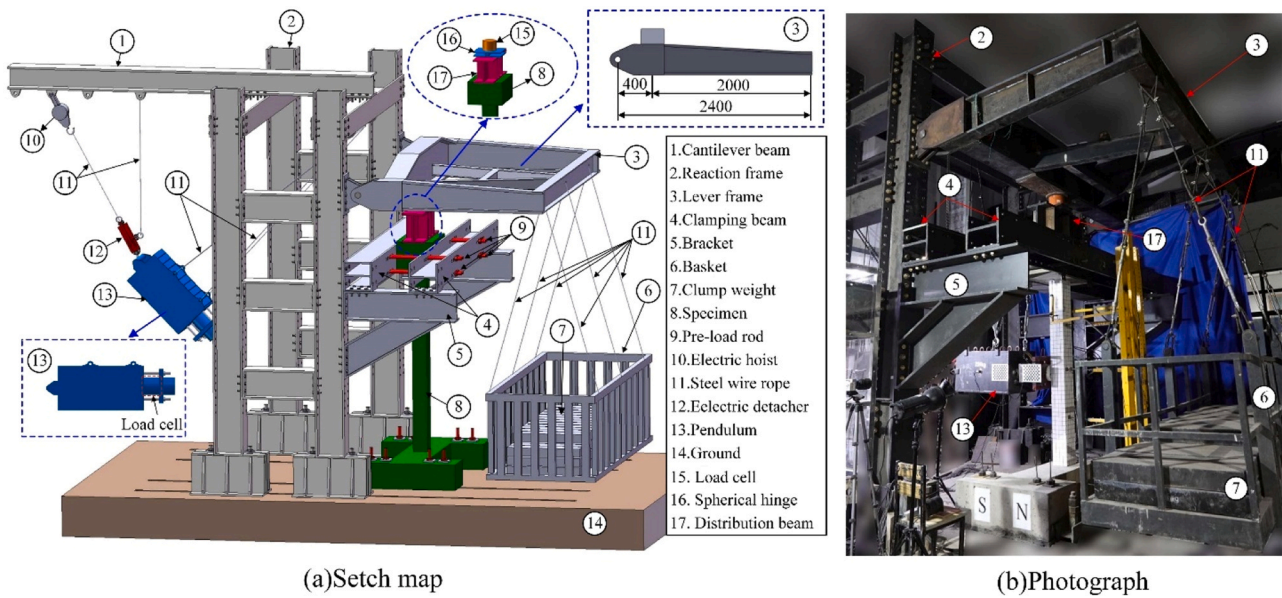Fig. 3 shows the test setup for the pendulum impact test, which

(a)Setch map

1.Cantilever beam
2.Reaction frame
3.Lever frame
4.Clamping beam
5.Bracket
6.Basket
7.Clump weight
8.Specimen
9.Pre-load rod
10.Electric hoist
11.Steel wire rope
12.Eelectric detacher
13.Pendulum
14.Ground
15. Load cell
16. Spherical hinge
17. Distribution beam

(b)Photograph

Fig. 3. Schematic representation of the pendulum impact test setup.
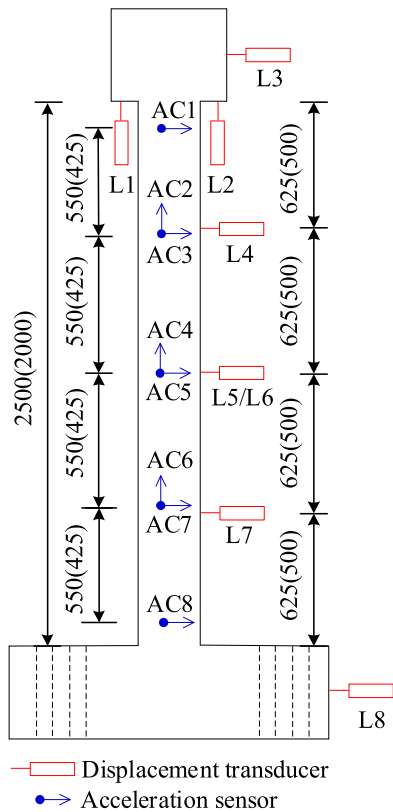

Fig. 4. Layout of the deformation and acceleration meter.

encompasses three primary parts: a vertical load application system, a stabilization framework, and a pendulum-based impact mechanism.

The vertical load application system includes a lever framework, a suspended container, and balancing weights. The system exerts vertical force using the leverage principle. In this system, the span from the fark end (holding the counterweight) of the lever structure to the pivot point (point of load application) is 5 times the distance from the revolute hinges to the pivot point (refer to Fig. 3a). In this test, the hanged basket was loaded with a counterweight of 7000 kg and suspended on the far

end of the lever frame using steel wire ropes. A spherical hinge was installed at the pivot point to facilitate the free rotation of the lever. A load cell was mounted at the center of the spherical hinge to measure the vertical pressure on the column.

The supporting framework is composed of a reaction frame, clamping beams, pre-load rods, and brackets. The foundation beam of each specimen was securely fixed in the laboratory's ground slot using eight screws. Polytetrafluoroethylene (PTFE) sheets were installed between the clamping beam and the top of the column to mitigate frictional resistance between them resulting from their relative motion in the vertical direction.

The pendulum impact mechanism consists of an electric detacher, an electric hoist, steel wire ropes hanging the pendulum, and the pendulum itself. The pendulum primarily consists of weights provided by steel plates and a hammerhead featuring a curved surface of 200 mm in diameter.

Fig. 4 illustrates the displacement and acceleration measurement point arrangement on the column specimens. Eight resistive displacement sensors (L1-L8) and eight piezoelectric acceleration sensors (AC1-AC8) were installed to measure horizontal and vertical displacements and accelerations. The acceleration sensors (KD10000A by KEDONG ELECTRONICS) featured a shock-type, single-axis (IEPE) configuration, with a measurement range of up to $\pm$ 10,000 g and a sensitivity of 0.05 pC/g. A contact-type velocity sensor (KDS-20 by KEDONG ELECTRONICS) was installed on the pendulum's hammerhead. It was primarily used to capture the velocity variations of the pendulum during impact, with a maximum measurement range of up to 10 m/s. The load cell (CLL-2000KNA by TML company) is positioned between the pendulum's counterweight and the hammerhead to measure the impact forces. This strain gauge type sensor features a sensitivity of 2.0 mV/V and can handle a maximum range of up to 2000 kN. The data sampling rate was set at 500 kHz. The low-pass filter in the data acquisition system was set to a cutoff frequency of 30 kHz to mitigate noise interference. In addition, a high-speed camera operating at 5000 frames per second was utilized to capture the intricate details of crack development within the column.
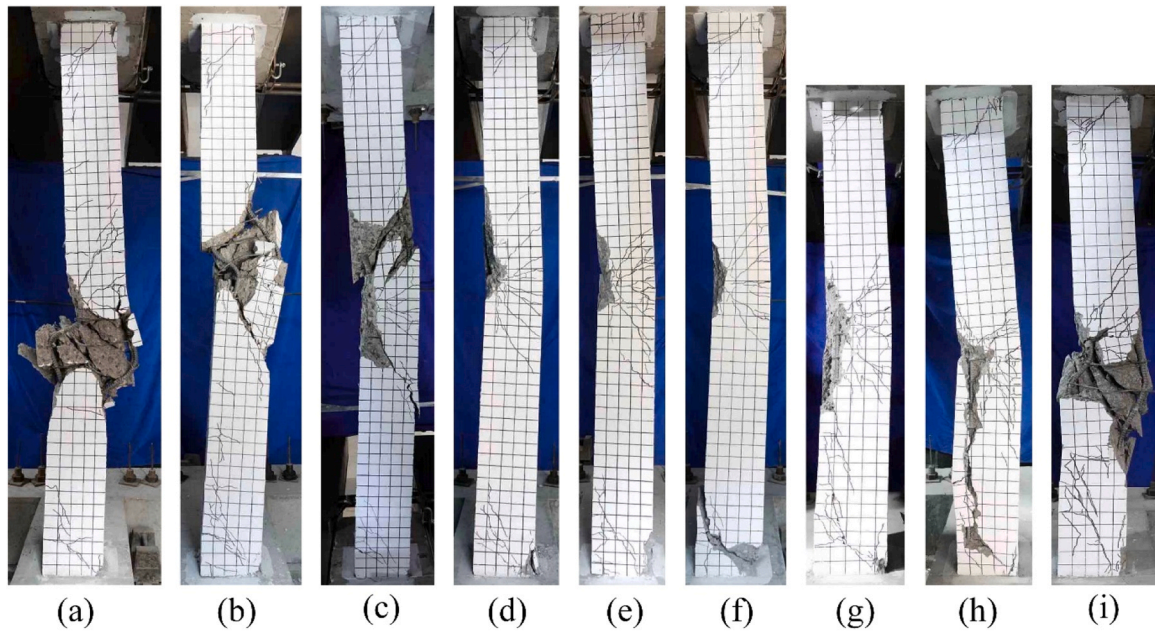
Fig. 5. Photographs of the specimens after impact: (a) C2.5-L-2167–4.71; (b) C2.5-L-1917–5.21; (c) C2.5-L-1667–5.71; (d) C2.5-H-2167–4.71; (e) C2.5-H-1917–5.21; (f) C2.5-H-1667–5.71; (g) C2-L-2167–4.71; (h) C2-L-1667–5.71; (i) C2-L-1417–6.21.
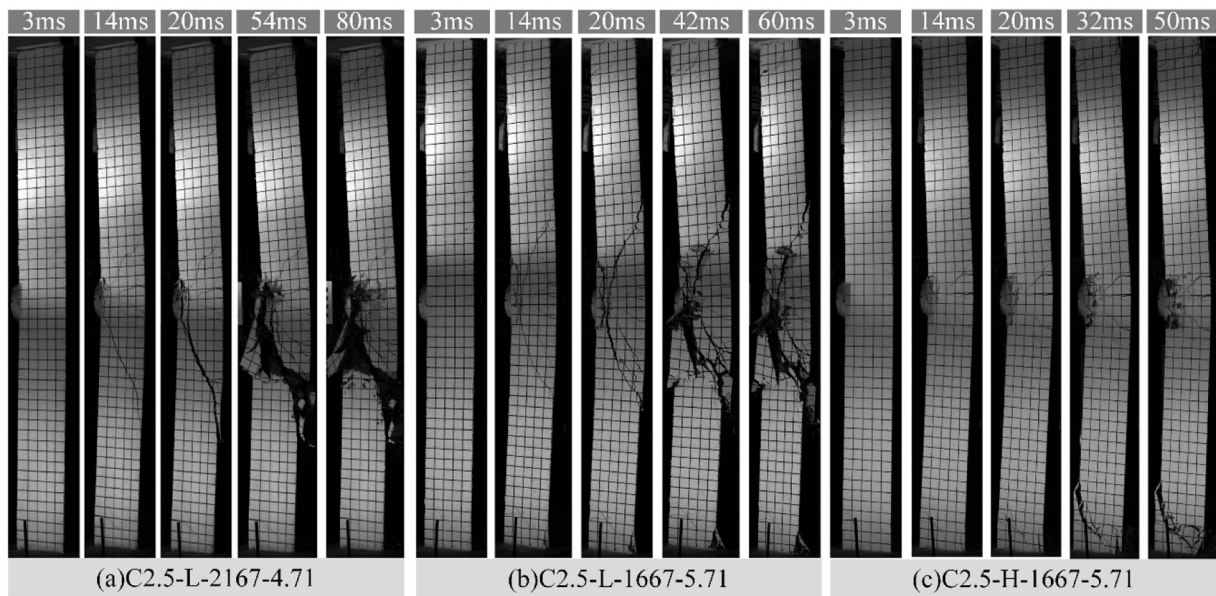

Fig. 6. Damage evolution of typical columns with various shear failure modes.

3. Test results

3.1. Failure mode and damage evolution

The final failure modes of the specimens are illustrated in Fig. 5. Specimens C2.5-L-2167–4.71 and C2-L-1417–6.21 experienced one-side shear failure, characterized by the presence of diagonal shear failure surfaces only on the side below the impact point, as shown in Fig. 5(a) and (i). Specimens C2.5-L-1917–5.21 and C2.5-L-1667–5.71 exhibited diagonal shear failure surfaces on both sides of the impact point, symmetrically aligned about the cross-section at the impact point, forming a shear plug, as depicted in Fig. 5(b) and (c). This type of shear failure mode is defined in this study as a two-side shear failure. Specimen C2.5-H-1667–5.71 also underwent shear failure, but the diagonal failure

surface was located in the negative bending moment region at the base of the column (Fig. 5(f)). Hence, it is classified as the end shear failure. Other specimens, including C2.5-H-2167–4.71, C2.5-H-1917–5.21, C2-L-2167–4.71, and C2-L-1667–5.71, did not exhibit significant failure surfaces after impact and were still capable of carrying vertical gravity loads. Hence, it was considered that these specimens underwent only impact damage without complete failure.

Utilizing the high-speed camera to capture the damage evolution process in the columns under impact loads is instrumental in identifying their impact failure modes. The images in Fig. 6 illustrate the specimens at different moments during the impact process exhibiting various shear failure modes. At the 3 ms after the column began to experience the impact load (close to the end of the initial peak phase of the impact force, as mentioned in Section 3.2), only minor diagonal cracks were
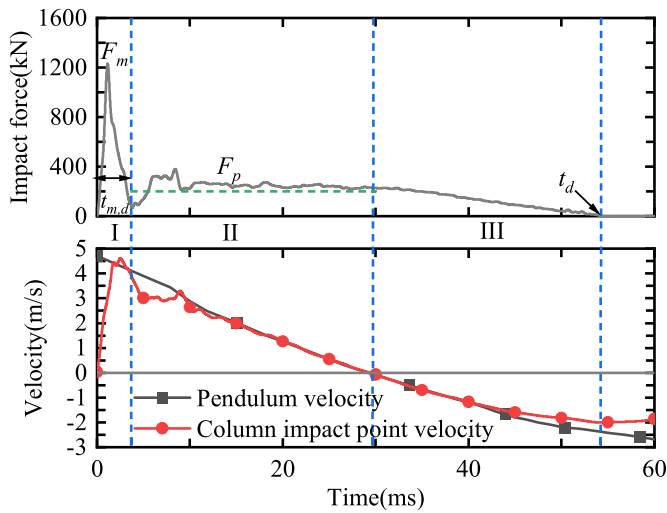
Fig. 7. Three phases of typical time-history curves (specimen C2.5-H-2167–4.71).

visible near the impact point and at the column ends, and the column deformation was also minimal. By 14 ms, the specimens C2.5-L-2167–4.71 and C2.5-L-1667–5.71 displayed significant critical diagonal cracks on both sides of the impact point, wider than other cracks. Subsequently, the critical diagonal crack beneath the impact point of specimen C2.5-L-2167–4.71 developed into a failure surface, accumulating most of the column's deformation and resulting in considerable concrete spalling near it, as depicted in Fig. 6(a). This represents the typical crack development and damage evolution process for the one-side shear failure of the specimens.

For specimen C2.5-L-1667–5.71, as shown in Fig. 6(b), the critical shear cracks on both sides of the impact point developed into failure surfaces by 14 ms, connecting to form a shear plug that began to detach

from the column. Subsequently, extensive concrete spalling occurred near both failure surfaces, indicating two-side shear failure of the column.

For specimen C2.5-H-1667–5.71, within the first 20 ms of the impact, the widest crack was consistently a bending crack located in the middle of the column, as shown in Fig. 6(c). At 32 ms, a wider critical diagonal crack appeared at the bottom of the column, eventually evolving into a shear failure surface. The delayed appearance of the failure surface in the column experiencing end shear failure might be related to the dynamic response of the column. This topic will be further discussed in Section 4.1.

3.2. Time history curves of impact force

During the test, the impact force at the position of the hammerhead was measured using a load cell, and the velocity of the columns at the impact point was obtained by integrating the data measured by the accelerometer AC5. The velocity of the pendulum was measured using a velocity sensor placed at the position of the hammerhead. Fig. 7 presents the typical time history curves for the impact force and velocities of the pendulum and the column at the impact point. Based on the interaction process between the pendulum and the column, the impact force time history curve can be divided into three phases: the initial peak phase (phase I), the overall response phase (phase II), and the pendulum-column separation phase (phase III) [22].

In phase I, i.e., immediately after the initial contact between the pendulum and the column, the pendulum began to decelerate, transferring kinetic energy to the column. At the same time, the impact force starts to propagate in the form of stress waves from the impact point toward both ends of the column. During this phase, the impact force exhibited a triangular pulse with the most significant peak value and a short duration. In the early period of phase II, due to the lateral stiffness of the column, its velocity rapidly decreased. With the re-contact between the pendulum and the column, a second peak value of the impact force was formed. Subsequently, the pendulum and the column moved
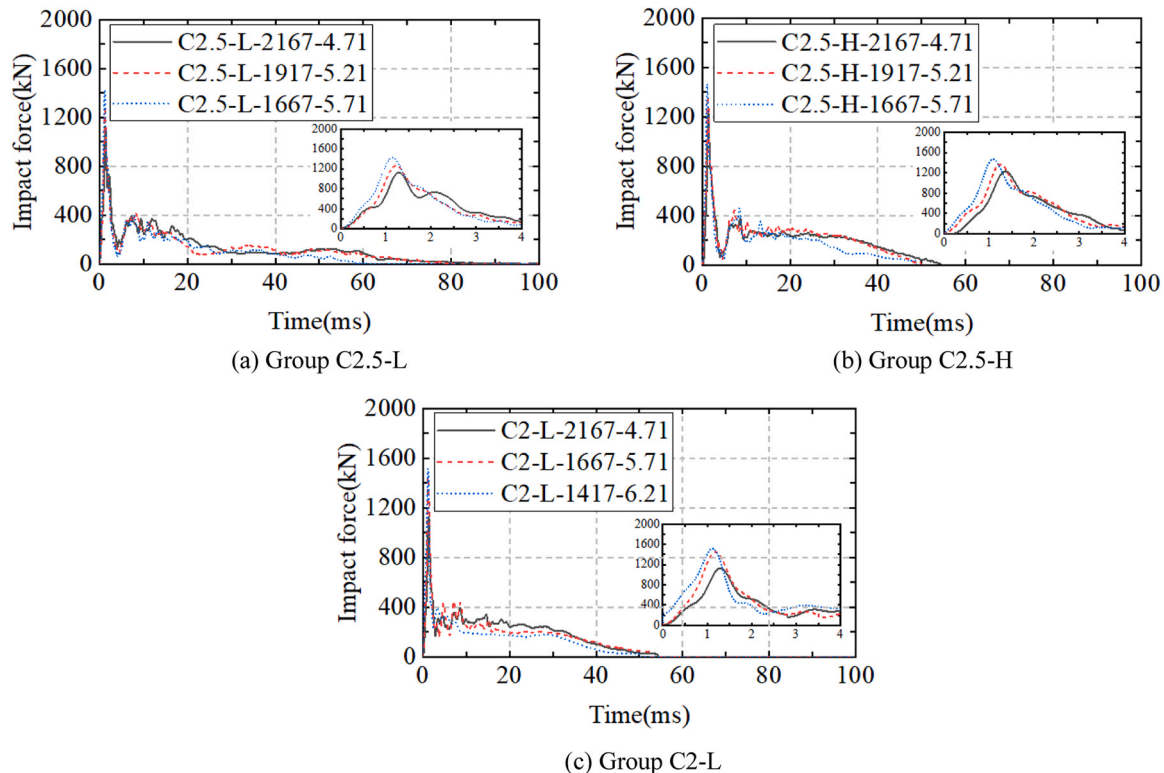

(a) Group C2.5-L

(b) Group C2.5-H

(c) Group C2-L

Fig. 8. Time history curves of impact force.

Table 2
Characteristic values for time history curves of impact force.

Group Number	Specimen No.	F_m (kN)	F_p (kN)	$t_{m,d}$ (ms)	t_d (ms)	D_m (mm)	D_r (mm)
C2.5-L	C2.5-L-2167-4.71	1128.5	160.7	4.01	80.21	79.5	68.1
	C2.5-L-1917-5.21	1260.1	154.6	3.88	70.23	96.7	81.5
	C2.5-L-1667-5.71	1428.3	140.4	3.65	58.91	77.8	64.4
C2.5-H	C2.5-H-2167-4.71	1230.3	245.5	3.69	54.22	65.6	37.9
	C2.5-H-1917-5.21	1370.8	237.4	3.41	49.95	67.4	35.3
	C2.5-H-1667-5.71	1468.1	223.6	3.22	48.79	72.7	55.5
C2-L	C2-L-2167-4.71	1132.1	272.4	2.82	54.19	56.5	29.5
	C2-L-1667-5.71	1446.4	243.2	2.64	52.32	70.9	45.2
	C2-L-1417-6.21	1519.1	204.5	2.32	49.92	70.5	51.6

Note: F_m represents the peak impact force; F_p represents the average value of the impact force during the Phase II; $t_{m,d}$ represents the duration of the peak impact force pulse, t_d represents the total duration of the impact force; D_m represents the peak displacement; D_r represents the residual displacement.

at the same velocity, and the impact force gradually stabilized at a relatively constant plateau value. In phase III, as the pendulum and the column began to separate, the impact force gradually decreased to zero, marking the end of the impact process.

Fig. 8 presents the time history curves of the impact forces applied to the specimens, with their first triangular pulses magnified for detailed

observation. The characteristic values of these curves are presented in Table 2. As can be seen from Fig. 8, in Phase I, the peak impact forces F_m of the specimens in each group increase with the rising impact velocity of the pendulum despite a reduction in the impact mass. The durations $t_{m,d}$ of the peak impact force pulse for the specimens in group C2-L are smaller than the other groups, possibly due to their larger lateral stiffnesses, shortening the initial contact durations. In Phase II, the average impact force F_p of the columns in each group decreases as the pendulum impact velocity increases, which might be attributed to the increased damage to the columns. Whereas, the variation in the total impact duration t_d follows a different trend from that of $t_{m,d}$. The durations t_d of the specimens in Groups C2.5-H and C2-L are noticeably shorter than those of Group C2.5-L, possibly due to their more excellent impact resistances.

3.3. Time history curves of horizontal displacement

Fig. 9 presents the horizontal displacement time history curves of the columns at the impact point, with the peak displacement D_m (during the impact) and the residual displacement D_r (after the impact) detailed in Table 2. It is evident that, in Phase I, the horizontal displacement of each specimen is small, and the differences among the specimens in each group are negligible. The peak horizontal displacement D_m occurred in Phase II of the impact, with columns that experienced shear failure showing more significant peak displacements than those that did not undergo shear failure. The residual displacement, D_r, exhibits a similar trend: D_r of the columns with impact damage are less than 50 mm, whereas the columns that underwent shear failure have D_r values exceeding 50 mm.
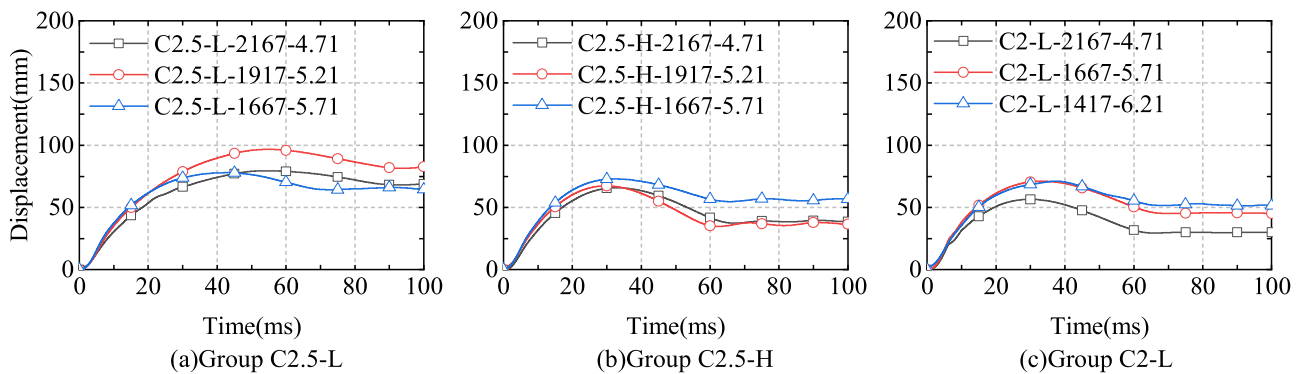

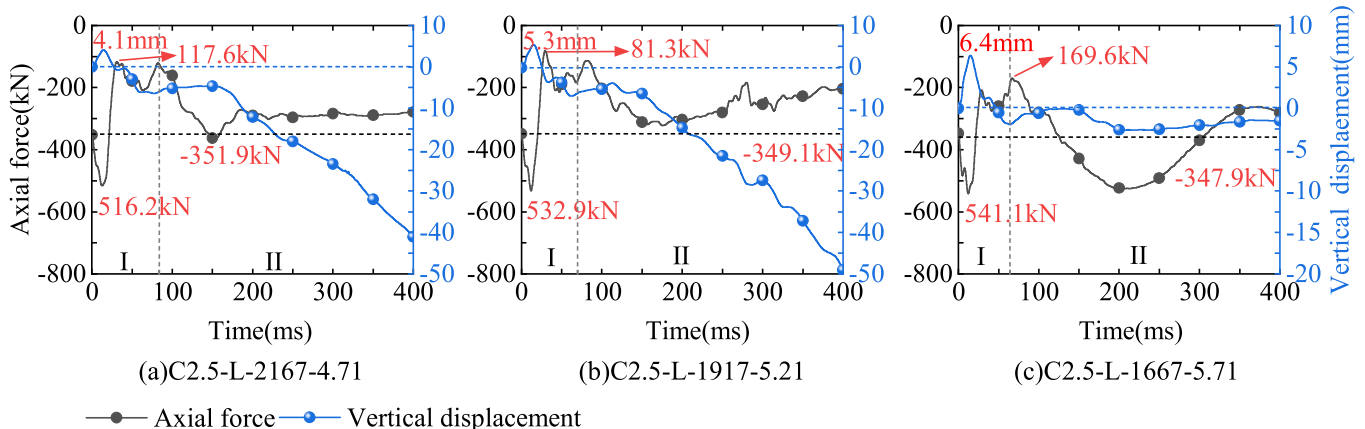**Fig. 9.** Horizontal displacement time history curves.

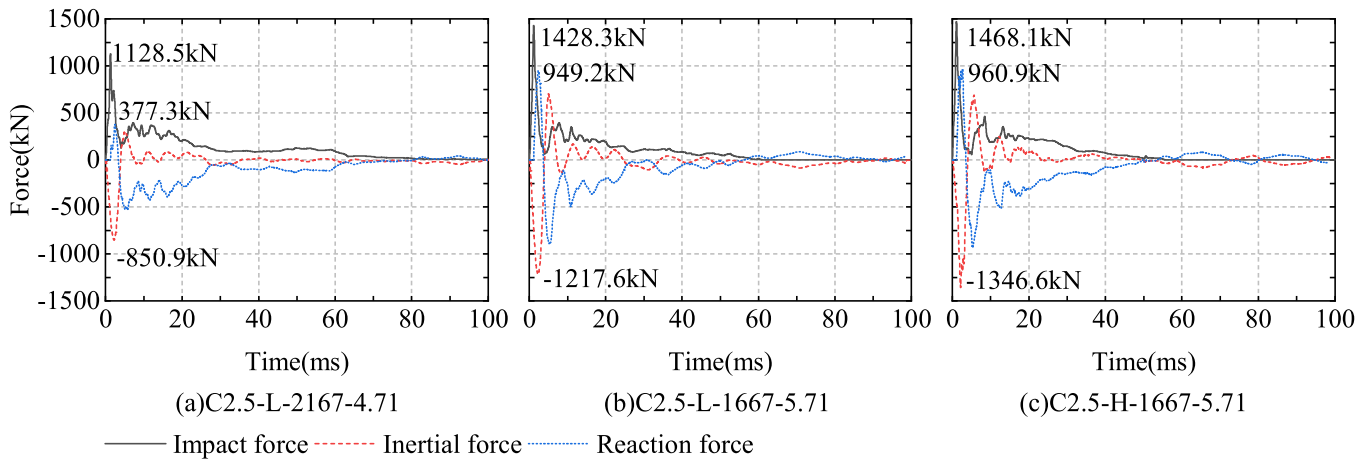**Fig. 10.** Time-history curves of axial force and vertical displacement for Group C2.5-L specimens.

Fig. 11. Time history curves of impact force, inertial force, and support reaction for selected columns.

3.4. Dynamic axial force and vertical displacement

Fig. 10 presents the time history curves of axial force and vertical displacement measured at the top of the columns in Group C2.5-L. It is observed that the axial force of each specimen increased from the initial value to the peak value in the early stage of impact ($t < 15$ ms). This is attributed to upward displacements of the column cap caused by the arching action. As the impact velocity increased from 4.71 to 5.71 m/s, the peak vertical displacement of the columns increased from 4.1 to 6.4 mm, while the axial compressive force also increased from 516.2 to 541.1 kN. It shows that the impact velocity or impact force influenced the axial force of the columns, and the axial force underwent significant changes during the impact process. This cannot be reflected by conventional axial loading methods like using a jack.

Subsequently, the axial force gradually tended to stabilize, and the vertical displacement of the column cap decreased simultaneously, showing negative values, indicating that the column height was lower than the initial value.

4. Failure mode transition analysis: from internal force and energy perspective

4.1. Internal force analysis

Under impact loads, the columns are subjected to the impact force, support reaction, and inertial force in the horizontal direction. These three forces satisfy dynamic equilibrium, assuming the damping effect during the impact is neglected. According to d'Alembert's principle, the sum of the impact force, inertia force, and support reaction equals zero. The support reaction was determined based on the measured impact force and the calculated overall horizontal inertia force (using the method described in references [34–37]).

The time history curves of the impact force, inertia force, and support reaction for selected columns are shown in Fig. 11. It is observed that the ratio of peak inertia force to the peak impact force ranges from 0.75 to 0.91, indicating that during the early stages of impact, the majority of the impact force was primarily resisted by the horizontal inertia force. In the later stages of the impact, as the inertia force rapidly diminished, the impact force was primarily balanced by the support reaction. Additionally, the time history curves of the support reaction reveal that due to the presence of the inertia force, the direction of the support reaction altered during the impact process. The appearance of support reaction in
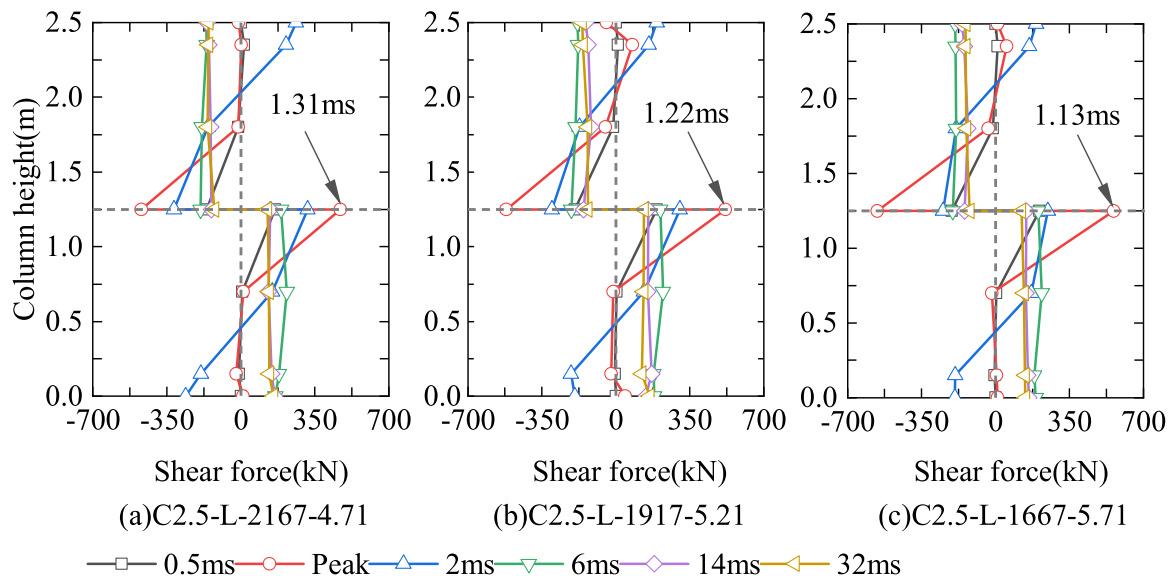

Fig. 12. Dynamic internal shear force distribution in Group C2.5-L columns.
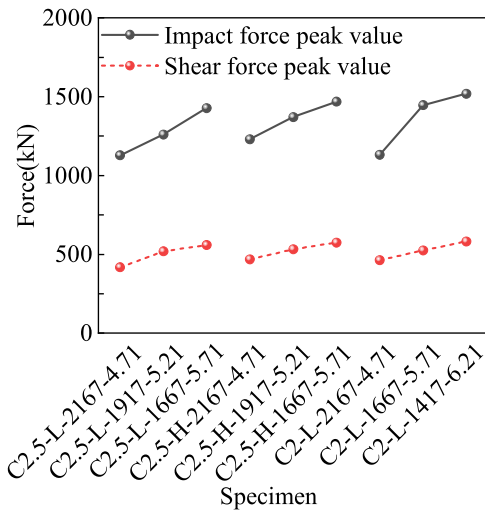
Fig. 13. Comparison of peak impact forces and peak shear forces for specimens.

line with the direction of the impact force in the early stage is caused by deformations related to higher-order mode shapes of the columns, which are controlled by the column's natural frequencies and the impact energy [38].

To determine the dynamic internal force distribution in the columns, it is assumed that the boundary conditions at the upper and lower ends are identical (rigidly fixed), resulting in equal support reactions at both ends. Fig. 12 illustrates the internal shear force distribution at different moments for the columns in Group C2.5-L. It is evident that during Phase I of the impact, significant variations occurred in the shear values concerning both position and time. This is attributed to the combined effect of dynamic impact forces and horizontal inertial forces. In this phase, the shear force at the impact point was considerably greater than those on other sections, showing a substantial difference in shear distribution compared to static conditions. This divergence might be a primary reason for the variation in failure modes of columns under impact loads compared to its static counterparts.

As illustrated in Fig. 12, when the impact velocity increases from 4.71 m/s to 5.71 m/s, the maximum shear force increases from 471.4 kN to 558.9 kN, indicating a rise of 18.4 %. The significant increase in impact velocity also elevates the strain rates of both concrete

and reinforcement, leading to an increase in resistance due to strain rate effects. Hence, the significantly increased shear force near the impact point and the improved column impact resistance with increasing impact velocity could explain the transition from one-side shear failure to two-side shear failure of the columns in this group.

Fig. 13 presents the relationship between the peak impact force and the peak shear force at the mid-height of each specimen. It is worth noting that with an increase in the impact velocity, despite a reduction in the impact mass, there is a significant increase in the peak impact force. Consequently, the peak shear force at the mid-height of the columns increases correspondingly. Considering the randomness of column resistance and actual boundary conditions, when the impact force or internal shear force reaches a specific value, a shear failure surface forms on one side of the impact point, resulting in the one-side shear failure of the columns. If the impact force or shear force continues to increase, critical shear cracks on both sides of the impact point develop into shear failure surfaces, leading to the two-side shear failure of the columns.

Fig. 14 shows the dynamic bending moment distribution for the Group C2.5-H columns. It can be observed that both maximum positive and negative bending moments increase with an increase in impact velocity. When the impact velocity increases from 4.71 m/s to 5.71 m/s, the maximum positive moment at the mid-height section of the columns increases from 142.3 to 189.8 kN·m, indicating a rise of 33.4 %.

At 32 ms of the impact (Phase II), the absolute value of the negative bending moment exceeded the positive bending moment, as shown in Fig. 14. When the impact velocity increased from 4.71 m/s to 5.71 m/s, the ratio of negative bending moment at the column end to the positive bending moment at mid-height increased from 1.2 to 1.4. This indicates that with the increase in impact velocity, the increase in the negative bending moment is more significant than that of the positive bending moment. As an increase in bending moment diminishes the shear capacity of RC members, the increased negative bending moment (at the column end) leads to a shift in shear failure from the mid-height to the end of the column. This explains the primary reason behind the occurrence of end shear failure in specimen C2.5-H-1667–5.7. The variation of the bending moment over time, as shown in Fig. 14, indicates that the shear failure at the column end occurred later than the shear failure near the impact point. This aligns with the sequence of crack development captured by the high-speed camera, as shown in Fig. 6.
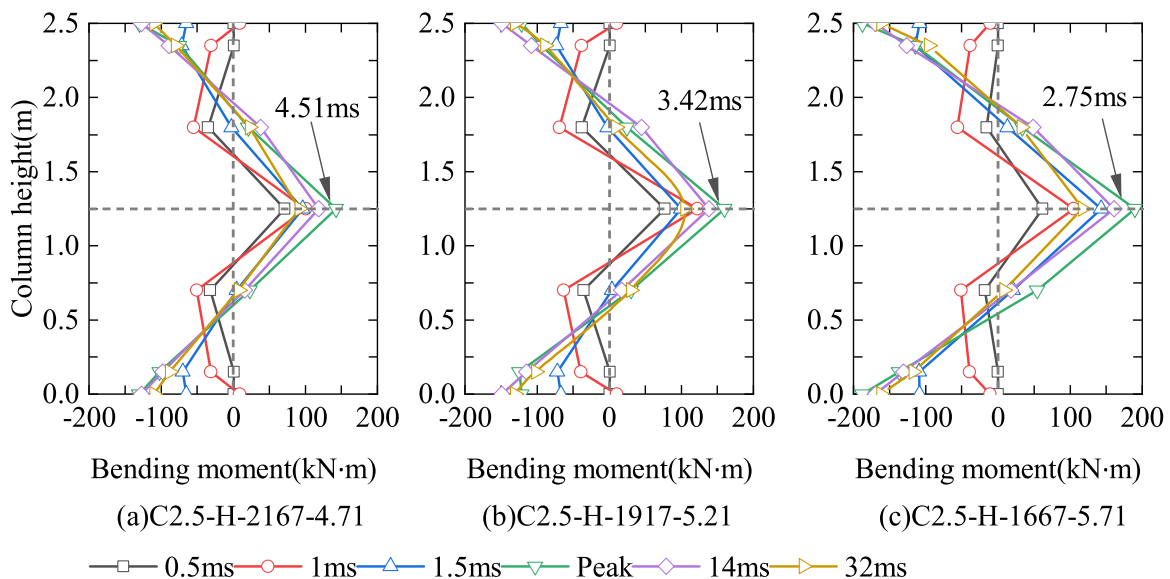

Fig. 14. Dynamic bending moment distribution in Group C2.5-H Columns.

Table 3
Energy dissipation values of each test specimen column.

Specimen No.	E_K (kJ)	E_V (kJ)	E_{TV} (kJ)	E_D (kJ)	$E_D/(E_K - E_V)$
C2.5-L-2167-4.71	24.04	5.53	2.23	16.28	0.88
C2.5-L-1917-5.21	26.02	5.74	2.78	17.50	0.86
C2.5-L-1667-5.71	27.18	8.96	3.21	15.01	0.82
C2.5-H-2167-4.71	24.04	8.36	2.45	13.23	0.84
C2.5-H-1917-5.21	26.02	8.85	2.51	14.66	0.85
C2.5-H-1667-5.71	27.18	9.03	2.58	15.57	0.86
C2-L-2167-4.71	24.04	9.19	1.67	13.18	0.89
C2-L-1667-5.71	27.18	9.27	1.88	16.03	0.90
C2-L-1417-6.21	27.32	7.87	2.68	16.77	0.86

4.2. Energy dissipation analysis

From the perspective of energy conversion, during the pendulum impact on the column, the energy transferred to the column primarily transformed into deformation energy E_D and kinetic energy E_{TV} (= horizontal kinetic energy + vertical kinetic energy). Assuming energy loss could be neglected, the change in kinetic energy of the pendulum during the impact process equals the sum of the deformation energy and kinetic energy of the column.

$$E_K - E_V = E_D + E_{TV} \tag{1}$$

where E_K and E_V represent the total and residual kinetic energy of the pendulum impact, namely the initial and rebound kinetic energy of the pendulum during the impact process, respectively. When calculating the column kinetic energy E_{TV}, the horizontal velocity V_H and vertical velocity V_V of the column were obtained by integrating the measured accelerations.

$$E_{TV} = \frac{1}{2}m_c[V_H^2(t) + V_V^2(t)] \tag{2}$$

$$V_H(t) = \int_0^t [A_1(t) + A_3(t) + A_5(t) + A_7(t) + A_8(t)]dt \tag{3}$$

$$V_V(t) = \int_0^t [A_2(t) + A_4(t) + A_6(t)]dt \tag{4}$$

where m_c denotes the column mass; A_1 to A_8 represent the acceleration measured by acceleration sensors AC1 to AC8, respectively.

The calculated values of the energies for the specimens are shown in Table 3. The ratio $E_D/(E_K - E_V)$ represents the energy absorption capacity of columns throughout the impact process. It is observed that for columns with the low stirrup ratio (Group C2.5-L and Group C2-L), the ratio $E_D/(E_K - E_V)$ decreases as the impact velocity increases. This indicates that with higher impact velocities, the columns suffer more severe damage (transitioning from impact damage to one-side shear failure for Group C2-L and from one-side shear failure to two-side shear failure for Group C2.5-L), indicating weaker energy absorption capacity. In the examination of bending failures, significant plastic deformation of longitudinal reinforcement plays a crucial role in energy dissipation [39]. Compared to one-sided shear failures, two-sided shear failures demonstrate a more concentrated crack distribution. In cases of two-sided shear failure, longitudinal reinforcement in undamaged areas exhibits less deformation, thereby contributing less to energy dissipation. However, increased deformation of stirrups within the damaged areas enhances local energy dissipation effects. Although stirrups aid in energy dissipation, their impact is generally less significant than that of longitudinal reinforcement, explaining why two-sided shear failures have lower energy absorption capabilities than one-sided shear failures. This observation aligns with findings from literature [19] on beam behavior under impact loads, which indicated that increased impact velocities intensify local deformations and reduce overall energy dissipation, leading to a shift from global to local failure modes. However, columns with the higher stirrup ratio (Group C2.5-H) did not exhibit similar trends.

The variation in the energy absorption capacity of the columns could be explained by the change in failure modes. As the plastic deformation of rebars in shear-controlled columns mainly concentrates near the diagonal failure surface, columns without shear failure distribute plastic deformation of rebars over a larger region. Therefore, the energy absorption capacity for columns with one-side shear failure is lower compared to columns in the same group without shear failure. Likewise, the energy absorption capacity of columns with two-side shear failure is lower than that of specimens in the same group with one-side shear failure.
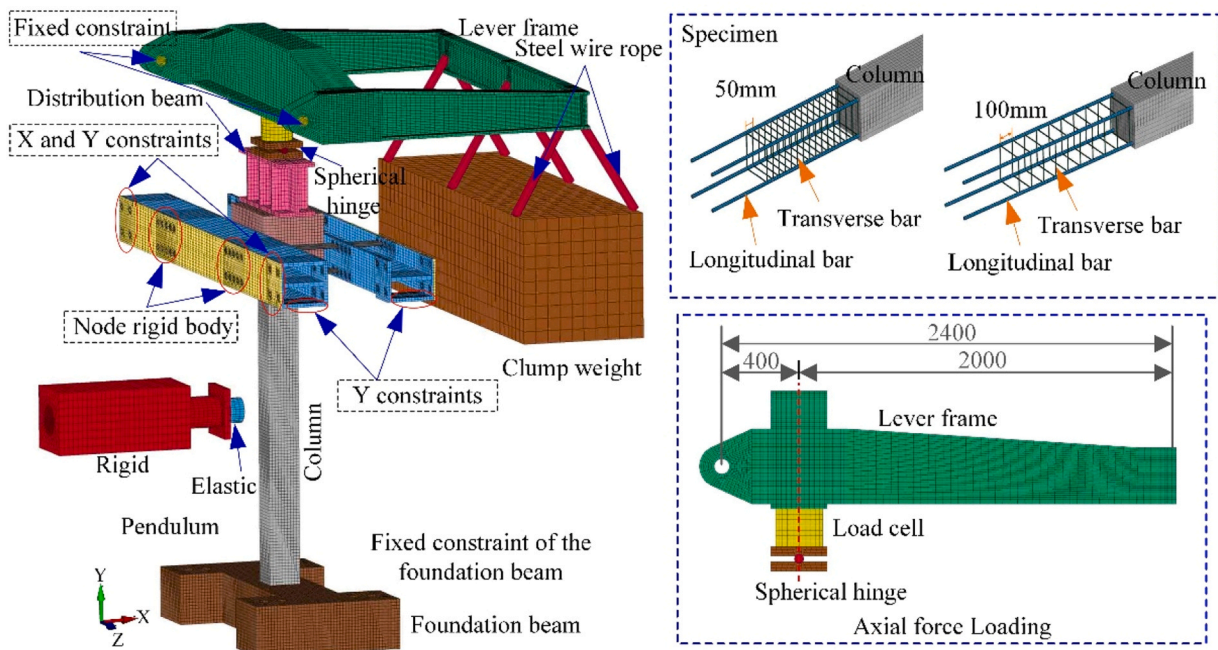

Fig. 15. Finite element model based on LS-DYNA.

Table 4
Material parameter values for various components.

Component	Material Keywords	Parameter Value
Pre-tensioned tie rod	CABLE_DISCRETE_BEAM	$\rho = 7850$ kg /m^3, $E = 195$ Gpa, $F_0 = 450$ kN
Steel wire rope	CABLE_DISCRETE_BEAM	$\rho = 7850$ kg /m^3, $E = 195$ GPa
Longitudinal reinforcement (25 mm)	PLASTIC_KINEMATIC	$\rho = 7850$ kg /m^3, $E = 206$ GPa, $v = 0.3$, $f_y = 443$ MPa, $E_t = 1.08$ GPa
Stirrup (12 mm)	PLASTIC_KINEMATIC	$\rho = 7850$ kg /m^3, $E = 206$ GPa, $v = 0.3$, $f_y = 490$ MPa, $E_t = 1.36$ GPa
Concrete	CSCM_CONCRETE	$\rho = 2400$ kg /m^3, FPC = 28.5 MPa, DAGG = 15 mm

5. Parametric analysis based on finite element method

Due to limitations in experimental conditions and costs, columns with high transverse reinforcement ratios were not tested with larger impact masses or velocities, and the impact capacities for different columns were not precisely equal. Additionally, as both impact velocity and mass were altered simultaneously during the test, the relationship between the peak impact force and the two parameters remained unclear.

To address these shortcomings in experimental research and to conduct comparative analyses over a broader parameter range, the finite element (FE) method was employed for parametric analysis under three scenarios: 1) increasing impact velocity under constant impact mass; 2) increasing impact mass under constant impact velocity; 3) increasing impact velocity and decreasing impact mass under constant impact energy.

5.1. Finite element modeling

Based on the LS-DYNA finite element software, a detailed nonlinear contact-collision FE model of RC columns was established, as shown in Fig. 15. Both the setup and the specimens were explicitly simulated using three-dimensional eight-node solid elements (SOLID). Steel rebars were modeled using two-node Hughes-Liu beam elements (BEAM). The prestressing system, including the pre-load rods (32 mm in diameter) and the steel wire ropes (30 mm in diameter) hanging the counterweight basket, were simulated using discrete beam/cable elements (DISCRETE BEAM/CABLE). After a mesh sensitivity analysis, a mesh size of 25 mm was determined to be optimal for both the steel reinforcement and
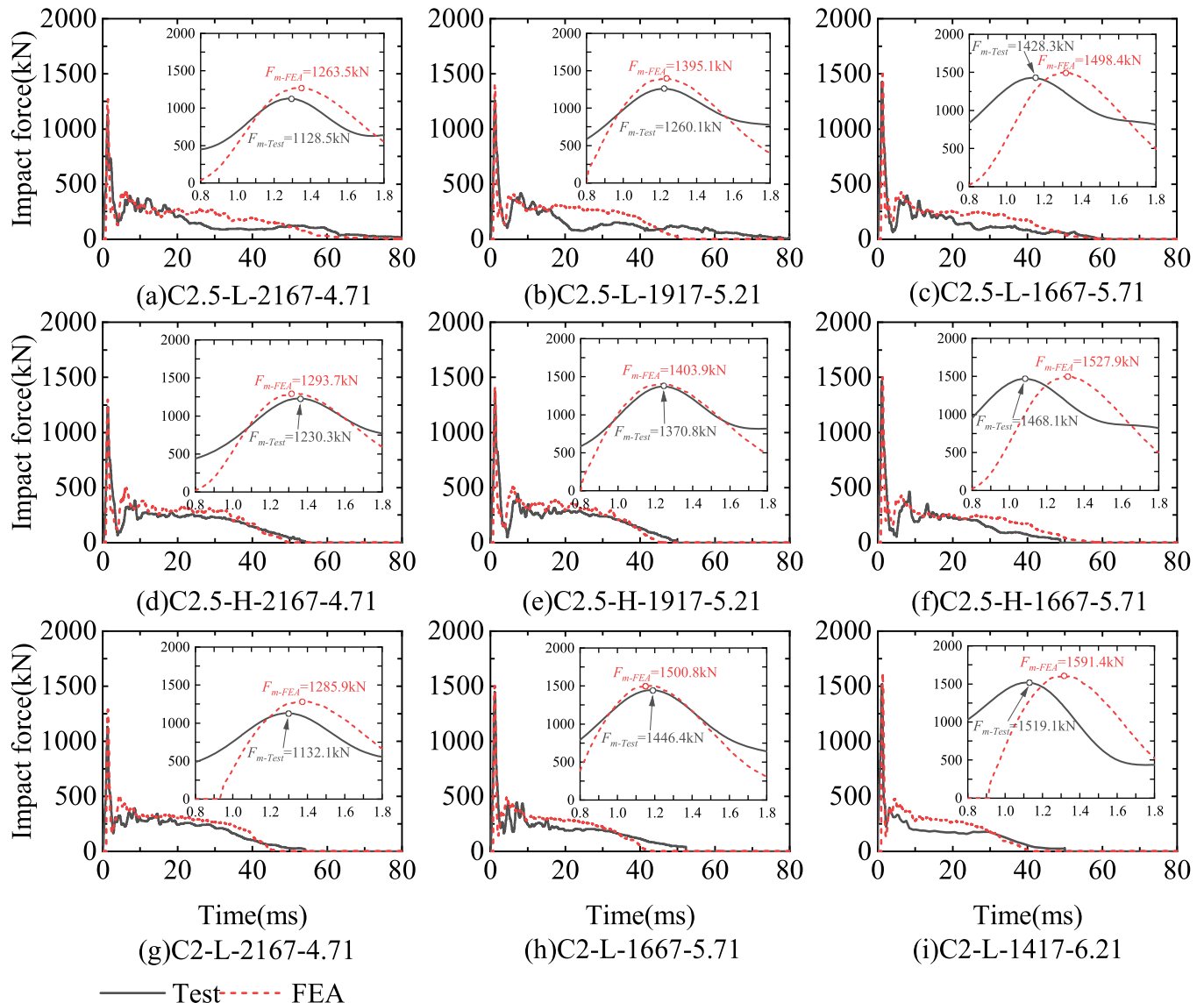

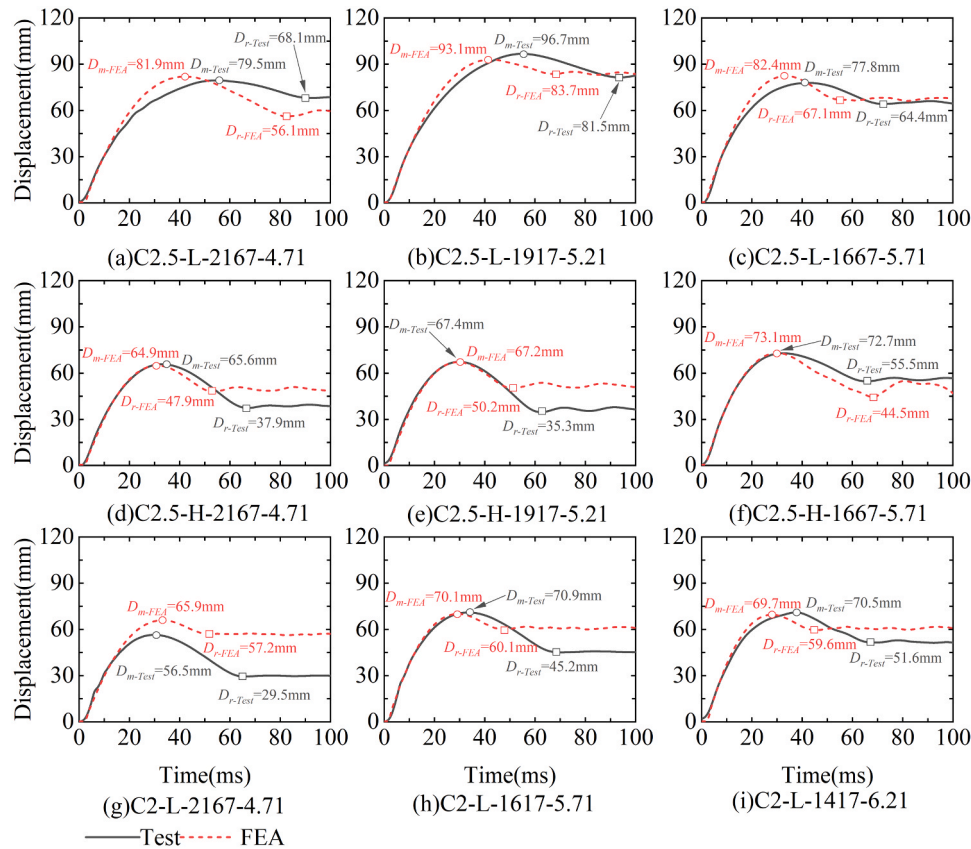**Fig. 16.** Impact force time curves by FE model and test.

Fig. 17. Horizontal displacement time curves by FE model and test.

concrete.

The reinforcements in columns were modeled using the PIECE-WISE_LINEAR_PLASTICITY material model, in which the constitutive curves of steel is determined according to experimentally measured stress-strain curves (Fig. 2). The material properties were set with a mass density (ρ) of 7850 kg/m^3, an elastic modulus (E) of 206 GPa, and a Poisson's ratio (μ) of 0.3. Strain rate parameters C and P were adopted as 7.274×10^7 and 11.22, respectively, based on references [40–42]. The CSCM model was adopted to simulate the concrete of the columns with the original version in which the default fracture energy was reasonably reduced [43]. Calibration of the CSCM model against experimental results showed that reducing the tensile fracture energy (GFT) and shear fracture energy (GFS) to 0.8 times their default values ($0.8GFT$ and $0.8GFS$) achieved a good match with the experimental results. Both the foundation beam and the column cap were modeled using CSCM_CONCRETE.

The pendulum hammerhead, lever frame pivot, lever frame, load cell, spherical hinge, distribution beam, and clamping beam were all simulated using the ELASTIC material model, with a mass density of 7850 kg/m^3, an elastic modulus of 206 GPa, and a Poisson's ratio of 0.3. The counterweights in the pendulum component were modeled using RIGID (as shown in Fig. 15), with the mass density calculated based on the actual mass-to-volume ratio of the counterweights, an elastic modulus of 206 GPa, and a Poisson's ratio of 0.3. The material parameters for other components are detailed in Table 4.

The initial impact velocity was applied to the pendulum using the keyword INITIAL_VELOCITY_GENERATION, and the gravitational field was applied to the entire model using LOAD_BODY_Y. The gravity loading involving initial preload axial force adjustment was realized by changing the density of the counterweights. Additionally, mass-weighted damping (GLOBAL_MASS_SET) was employed to control the vertical compression [44–47]. Due to the axial force being applied

suddenly before stabilization, the concrete may fail due to the abrupt loading, leading to a degree of inertial effects that ultimately affect the computational results of the model. To avoid oscillations caused by the sudden application of axial force and to incorporate the axial force into the transient dynamic analysis, Therefore, this study employs the mass-weighted damping method (GLOBAL_MASS_SET) to control the application of axial force. The primary goal of this method is to shorten the time required to reach static equilibrium while introducing damping variations [46,47]. At the start of the finite element simulation, damping is applied along with gravity loads. Once the preload axial force is reached, the damping is removed, ensuring that the axial force in the system is balanced before the pendulum impact. For more details, please refer to literature [47]. In the column caps and foundation beams, the connection between steel reinforcement and concrete is tied using the CONSTRAINED_BEAM_IN_SOLID method. As detailed in reference [48–51], this approach utilizes shared nodes, which not only enables precise prediction of diagonal shear cracks but also effectively simulates the dynamic responses of the components. Therefore, this study also employs shared node technology to accurately model the interactions between the reinforcement and concrete within the columns.

Contacts between the pendulum, the column, and other components were defined using the keyword AUTO_SURFACE_TO_SURFACE. The lever frame, steel wire ropes, and counterweights were connected using shared nodes. The pivot of the lever frame was set with fixed constraints, while the bottom and top positions of the clamping beam were respectively constrained in the Y direction, and in both X and Y directions, as shown in Fig. 15. The bottom of the foundation beam was fixed on all directions at locations of eight fixing screws.

5.2. Model validation

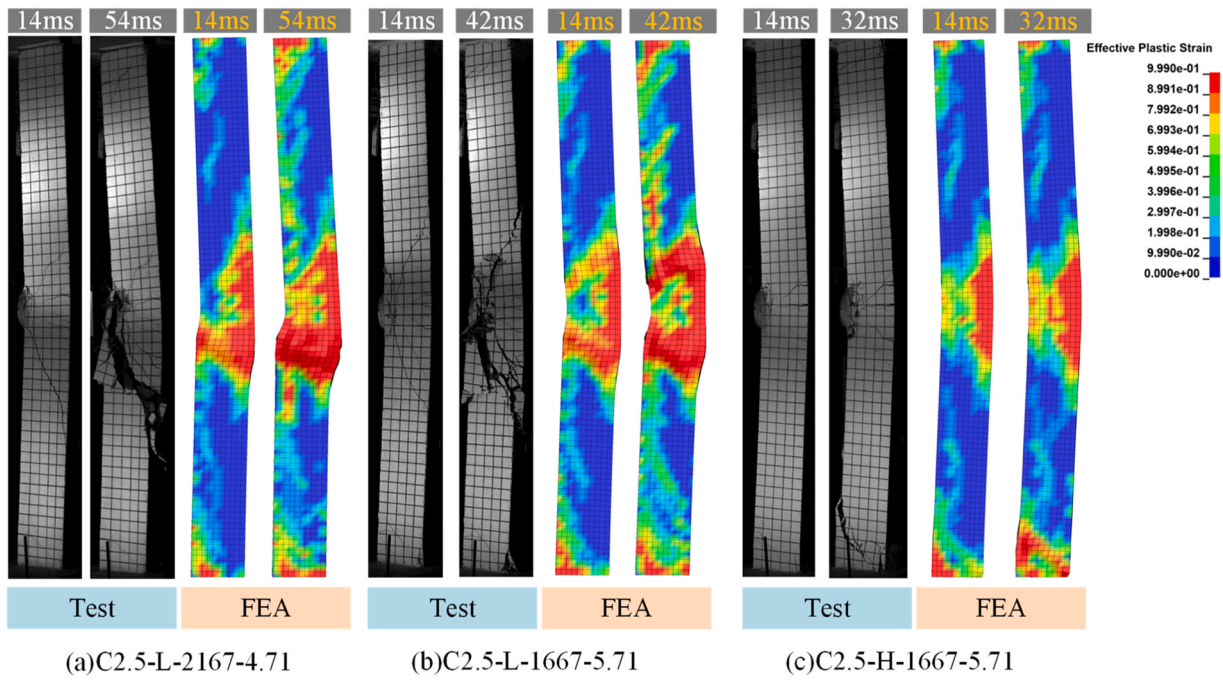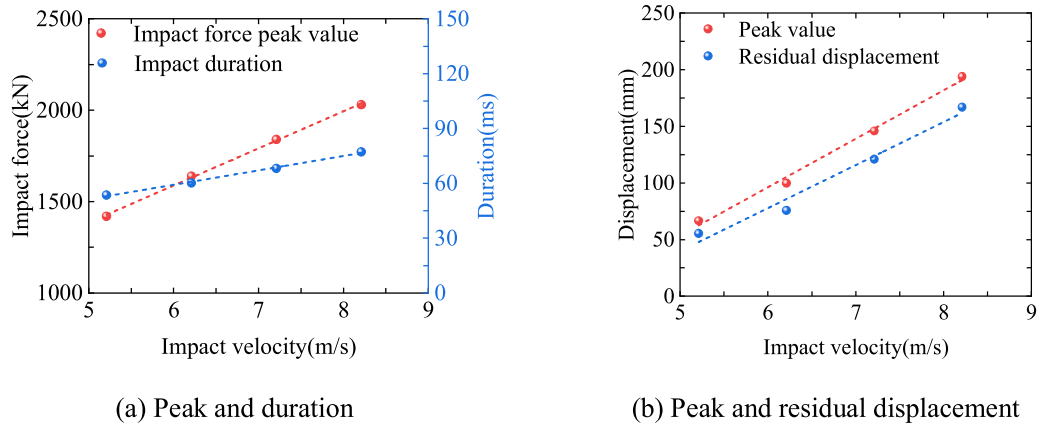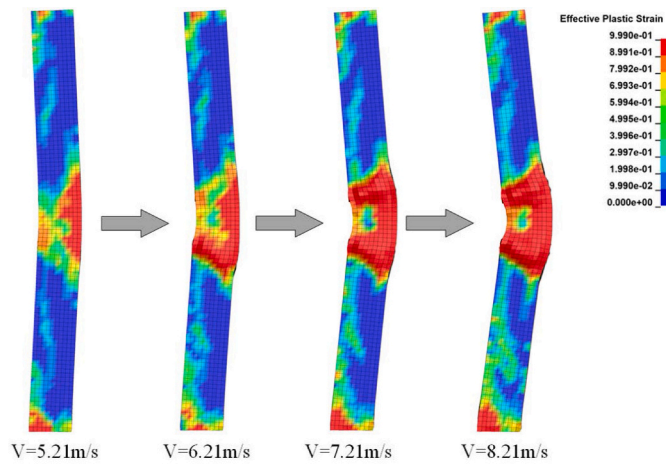Comparisons between the numerical and experimental results are

Fig. 18. Damage evolution and failure mode by FE model and test.

(a) Peak and duration

(b) Peak and residual displacement

(c) Failure modes represented by effective plastic strains

Fig. 19. Numerical results of columns with increasing impact velocity and constant impact mass.

(a) Peak and duration

(b)Peak and residual displacement

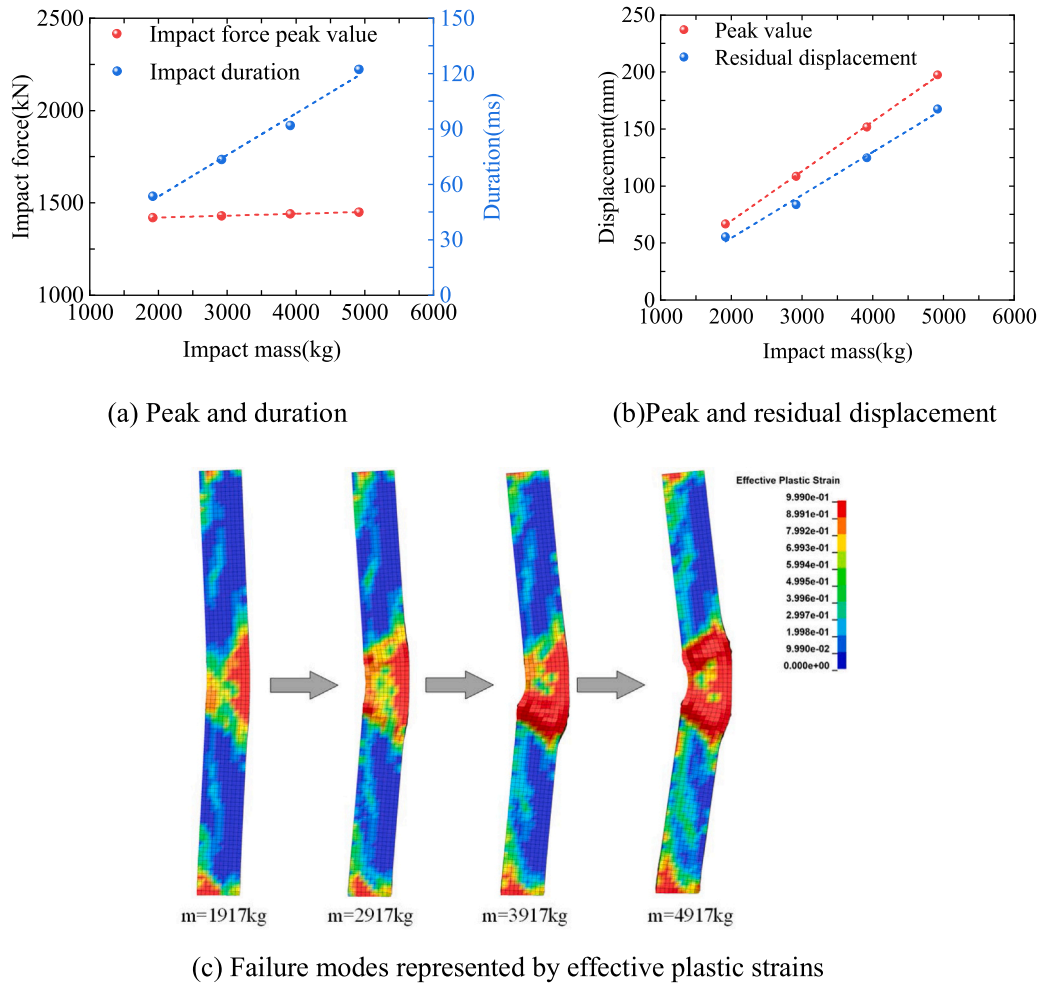(c) Failure modes represented by effective plastic strains

Fig. 20. Numerical results of columns with increasing impact mass and constant impact velocity.

shown in Figs. 16–18. As seen in Fig. 16, there is good agreement between the numerical and experimental results in the impact force time history curves. To properly simulate the peak impact force, which is closely related to the initial contact stiffness, the contact stiffness was calibrated by adjusting the penalty factors SFS and SFM in the contact parameters, as suggested by Pham et al. [52]. As shown in Fig. 16, the comparison error range between the simulated and experimental peak impact forces for all specimens is about 2.4 % to 11.9 %. This error may be attributed to deviations in the contact area of each specimen caused by the deflection of the pendulum during the impact in the experiment. However, this level of error is within an acceptable range.

Fig. 17 shows the horizontal displacement (at column mid-height) time history curves comparison on the test and FE results. It is evident that, before reaching the peak displacement, the numerical results align well with the experimental results. The simulation results for the peak values show an average error of 3.7 %. In the descending phase (residual displacement), the error is larger, with an average error of 28.4 %. This may not only be related to the constitutive characteristics of the CSCM model but may also be associated with the bond-slip behavior between the concrete and reinforcement [20].

Fig. 18 demonstrates that the FE model can reasonably predict the damage evolution and failure modes of the columns, such as the one-side shear failure in Fig. 18 (a), two-side shear failure in Fig. 18 (b), and end shear failure in Fig. 18 (c). From these comparative results, it could be deemed that the FE model can properly simulate the dynamic responses of the RC columns under impact.

5.3. Parametric analysis

The following parametric analysis was conducted using the validated FE model. For each set of parametric analyses, the first column (control specimen) is the FE model of specimen C2.5-H-1917–5.21, which was damaged under impact but did not fail in shear in the test. It should be noted that, for better identification and comparison of the column failure modes, the effective plastic strain contours were extracted at the end of the impact force plateau phase (Phase II).

5.3.1. Increasing impact velocity with constant impact mass

Fig. 19 shows the dynamic responses and the failure modes of the columns resulting from an increase in impact velocity (from 5.21 to 8.21 m/s) at the same impact mass (1917 kg). As can be seen from Fig. 19 (a) and (b), with the increase in impact velocity, there is a linear growth trend in peak impact force, duration, peak displacement, and residual displacement, in which the increases magnitudes being 43.1 %, 44.1 %, 190.9 %, and 201.4 %, respectively. From Fig. 19 (c), it can be observed that with the increase in impact velocity, the failure mode evolved from impact damage (without failure) to one-side shear failure and then to two-side shear failure.

5.3.2. Increasing impact mass with constant impact velocity

Fig. 20 demonstrates the dynamic responses and the failure modes of the columns with increased impact mass (from 1917 to 4917 kg) at a constant impact velocity of 5.21 m/s. With the increase in impact mass, impact duration, peak displacement, and residual displacement significantly increased by 128.25 %, 196.1 %, and 203.2 %, respectively.

(a) Peak and duration   (b) Peak and residual displacement

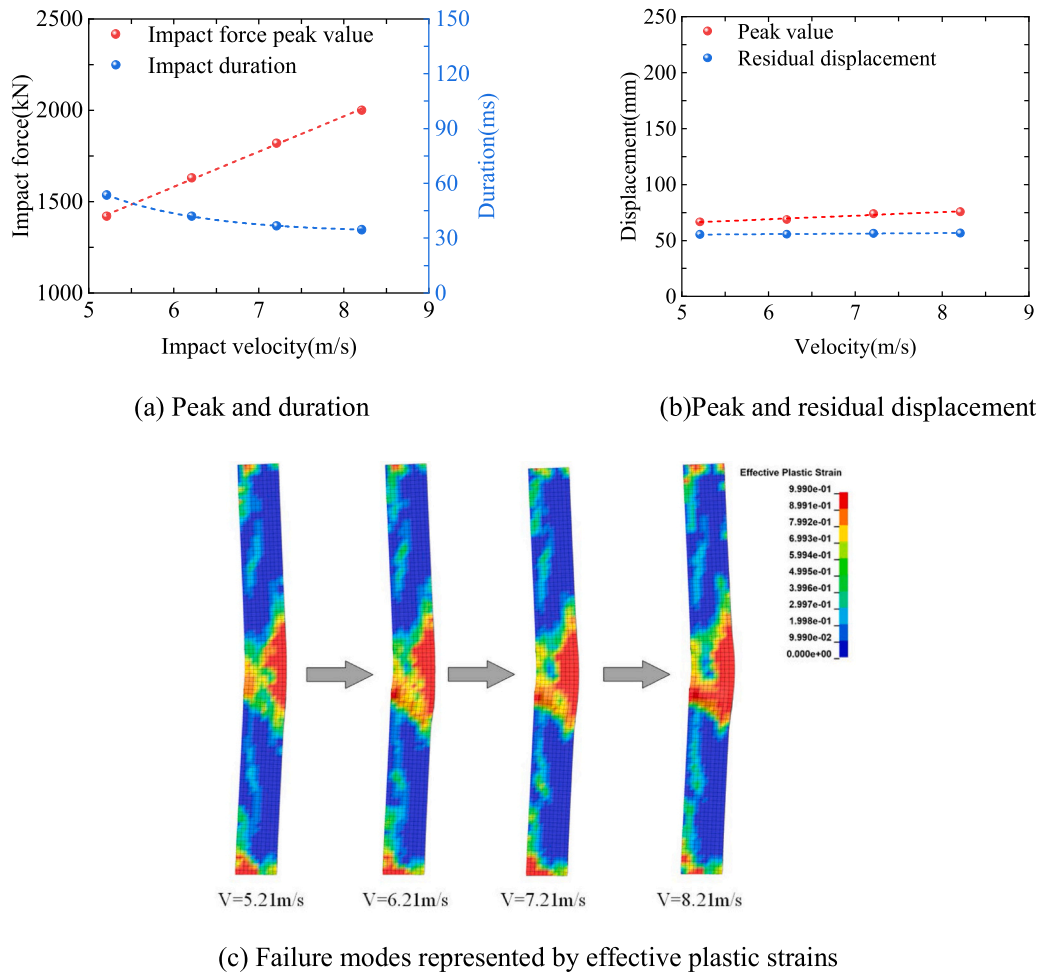(c) Failure modes represented by effective plastic strains

Fig. 21. Numerical results of columns with increasing impact velocity and constant impact energy.

However, the peak impact force remained almost unchanged (only a 2.12 % increase). The failure mode of the columns also transitioned from impact damage to one-side shear failure and then to two-side shear failure.

5.3.3. Increasing impact velocity with constant impact energy

Fig. 21 presents the dynamic responses and the failure modes of the columns under the same impact energy (26.02 kJ), with increased impact velocity (from 5.21 to 8.21 m/s) and correspondingly reduced impact mass (from 1917 to 772 kg). With the increase in impact velocity, the peak impact force shows a linear increase, with a growth of 40.8 %, while the duration decreases by 35.1 %. The increases in peak displacement and residual displacement are 13.5 % and 2.4 %, respectively. Fig. 21 (c) indicates that the increase in impact velocity led to a transition in the column failure mode from impact damage to one-side shear failure.

5.3.4. Discussion on parametric analysis results and recommendations for impact-resistant design

From the above three sets of parameter analyses, it can be concluded that maintaining the impact mass while increasing the impact velocity or maintaining the impact velocity while increasing the impact mass can trigger shear failure in the column, transitioning from one-side shear failure to two-side shear failure. When the impact energy is constant, increasing the impact velocity while reducing the impact mass exacerbates the impact damage to the column, potentially leading to shear failure.

The comparison of the parameter analyses reveals that the increase

in peak impact force is mainly caused by the increase in impact velocity, and it is not significantly related to the variation in impact mass. Higher peak impact force exacerbates column damage, transitioning from impact damage to one-side shear failure and further to two-side shear failure. However, the failure mode transition might not necessarily be caused by the increase in peak impact force (or impact velocity) but could also be attributed to the increase in impact energy (or impact mass).

Parametric analysis using finite element methods indicates that impact energy alone does not directly determine the impact load on RC columns; the specific combinations of impact mass and velocity also play a crucial role. Therefore, in the impact-resistant design of RC columns, when the external impact energy is fixed, it is essential to consider the potential increase in impact force caused by higher impact velocities. This consideration ensures the design accommodates various dynamic load scenarios effectively.

6. Summary and conclusion

Based on the pendulum impact tests and numerical parameter analysis conducted in this study, the effects of impact mass and velocity on the failure modes of RC columns with different stirrup ratios and slenderness ratios were investigated. The study delineates the following key conclusion:

1. The tests unveiled three distinct shear failure modes: one-side shear failure, two-side shear failure near the impact point, and shear failure at the column end. Increasing the stirrup ratio and reducing the

slenderness ratio is of significance to the enhancement of the impact resistance of RC columns.

2. Dynamic internal forces within the columns during impact were analyzed. The rise in peak impact force, consequently amplifying the peak shear force at the impact point, appeared to be the primary cause for the transition from impact damage to one-side shear failure and subsequently to two-side shear failure in columns with the low stirrup ratio. For the columns with the high stirrup ratio, the ratio of the negative bending moment (absolute value) at the column end to the positive bending moment at the mid-height increased with the increase of impact velocity, which might be the main reason for the shift of shear failure from the mid-height to the end of the column.

3. The columns with the low stirrup ratio demonstrated intensified and localized damage with increasing impact velocity, leading to a diminished energy absorption capacity. This phenomenon was associated with concentrated plastic deformation of reinforcement along the diagonal failure surface under shear failure.

4. The parametric analysis based on the FE method indicates that under conditions where impact mass remained constant while impact velocity increased, or when impact velocity remained constant while impact mass increased, shear failure could be triggered in the columns with high stirrup ratios, and the failure mode transitions from one-side shear failure to two-side shear failure. When the impact energy was kept constant, increasing the impact velocity while reducing the impact mass also induced shear failure in the columns.

5. The transition of failure modes in RC columns under impact loads was found to be influenced not only by peak impact force but also by process-related factors such as impact energy. Thus, in structural design and damage assessment of RC columns exposed to impact loads, consideration beyond mere focus on the peak impact force or the peak internal force becomes imperative.

CRediT authorship contribution statement

Hui Chen: Writing – review & editing, Methodology, Funding acquisition. **Jing-Ming Sun:** Writing – original draft, Visualization, Validation, Software, Methodology, Investigation, Data curation. **Wang-Xi Zhang:** Writing – review & editing. **Wei-Jian Yi:** Writing – review & editing, Supervision, Project administration, Conceptualization. **Yun Zhou:** Writing – review & editing, Supervision. **Qing-Feng He:** Writing – review & editing. **Fan Yi:** Writing – review & editing, Data curation. **Ya-Bo Ding:** Investigation.

Declaration of Competing Interest

The authors declared that they have no conflicts of interest to this work.

Data Availability

Data will be made available on request.

References

[1] Demartino C, Wu JG, Xiao Y. Response of shear-deficient reinforced circular RC columns under lateral impact loading. Int J Impact Eng 2017;109:196–213.

[2] Sha YY, Hao H. Laboratory tests and numerical simulations of CFRP strengthened RC pier subjected to barge impact load. Int J Struct Stab Dy 2015;15:1450037.

[3] Zhao WC, Ye JH, Qian J. Dynamic behavior and damage mechanisms of reinforced concrete piers subjected to truck impact. Eng Fail Anal 2021;121:105158.

[4] Heng K, Li R, Li Z, Wu H. Dynamic responses of highway bridge subjected to heavy truck impact. Eng Struct 2021;232:111828.

[5] Chen TL, Wu H, Fang Q. Dynamic behaviors of double-column RC bridge subjected to barge impact. Ocean Eng 2022;264:112444.

[6] Chen TL, Wu H, Fang Q. Impact force models for bridge under barge collisions. Ocean Eng 2022;259:111856.

[7] Fan W, Shen D, Huang X, Sun Y. Reinforced concrete bridge structures under barge impacts: FE modeling, dynamic behaviors, and UHPFRC-based strengthening. Ocean Eng 2020;216:108116.

[8] Nagata M, Beppu M, Ichino H, Takahashi J. Method for evaluating the displacement response of RC beams subjected to close-in explosion using modified SDOF model. Eng Struct 2018;157:105–18.

[9] Zhao D, Huang Y, Chen X, Han K, Chen C, Zhao X, et al. Numerical investigations on dynamic responses of subway segmental tunnel lining structures under internal blasts. Tunn Undergr Space Technol 2023;135:105058.

[10] Pham TM, Hao H. Effect of the plastic hinge and boundary conditions on the impact behavior of reinforced concrete beams. Int J Impact Eng 2017;102:74–85.

[11] Fujikake K, Li B, Soeun S. Impact response of reinforced concrete beam and its analytical evaluation. J Struct Eng 2009;135:938–50.

[12] Zhao W, Qian J. Dynamic response and shear demand of reinforced concrete beams subjected to impact loading. Int J Struct Stab Dy 2019;19:1950091.

[13] Zhong JH, Song CM, Xu JW, Cheng YH, Liu F. Experimental and numerical simulation study on failure mode transformation law of reinforced concrete beam under impact load. Int J Impact Eng 2023;179:104645.

[14] Zhang JF, Tong CK, Feng L, Du W, Wu FW. Evaluation and degradation mechanism of residual performance of RC beam after drop hammer impact. Int J Impact Eng 2022;169:104335.

[15] Fan W, Liu B, Huang X, Sun Y. Efficient modeling of flexural and shear behaviors in reinforced concrete beams and columns subjected to low-velocity impact loading. Eng Struct 2019;195:22–50.

[16] Liao WZ, Liu KX, Ma C, Liang JC. Experimental study on consistency of the impact performance between composite beams and reinforced concrete beams. Compos Struct 2023;308:116677.

[17] Sharma A, Ožbolt J. Influence of high loading rates on behavior of reinforced concrete beams with different aspect ratios - a numerical study. Eng Struct 2014; 79:297–308.

[18] Selcuk S, Frank JV. Effects of shear mechanisms on impact behavior of reinforced concrete beams. Acids Struct J 2009;106:78–86.

[19] Zhao DB, Yi WJ, Kunnath SK. Shear mechanisms in reinforced concrete beams under impact loading. J Struct Eng 2017;143:04017089.

[20] Liu B, Fan W, Guo W, Chen B, Liu R. Experimental investigation and improved FE modeling of axially-loaded circular RC columns under lateral impact loading. Eng Struct 2017;152:619–42.

[21] Gurbuz T, Ilki A, Thambiratnam DP, Perera N. Low-elevation impact tests of axially loaded reinforced concrete columns. Acids Struct J 2019;116:117–28.

[22] Sun JM, Yi WJ, Chen H, Peng F, Zhou Y, Zhang WX. Dynamic responses of RC columns under axial load and lateral impact. J Struct Eng 2023;149:04022210.

[23] Li RW, Zhou DY, Wu H. Experimental and numerical study on impact resistance of RC bridge piers under lateral impact loading. Eng Fail Anal 2020;109:104319.

[24] Cai J, Ye JB, Chen QJ, Liu XP, Wang YQ. Dynamic behaviour of axially-loaded RC columns under horizontal impact loading. Eng Struct 2018;168:684–97.

[25] Huang ZJ, Chen WS, Hao H, Siew AU, Huang TR, Ahmed M, Pham TM. Lateral impact performances of geopolymer concrete columns reinforced with steel-BFRP composite bars. Constr Build Mater 2024;411:134411.

[26] Li RW, Zhang N, Wu H. Effectiveness of CFRP shear-strengthening on vehicular impact resistance of double-column RC bridge pier. Eng Struct 2022;266:114604.

[27] Zhang XH, Hao H, Li C. Experimental investigation of the response of precast segmental columns subjected to impact loading. Int J Impact Eng 2016;95:105–24.

[28] Jin L, Zhang X, Zhang RB, Du XL. Numerical evaluation of impact resistance of concrete columns reinforced with GFRP bars under various axial force ratios and impact velocities. Eng Struct 2023;278:115501.

[29] Zhao WC, Ye JH. Dynamic behavior and damage assessment of RC columns subjected to lateral soft impact. Eng Struct 2022;251:113476.

[30] Sohel KMA, Al-Jabri K, Al Abri AHS. Behavior and design of reinforced concrete building columns subjected to low-velocity car impact. Structures 2020;26:601–16.

[31] Fu YQ, Yu XL, Dong XL, Zhou FH, Ning JG, Li P, Zheng YX. Investigating the failure behaviors of RC beams without stirrups under impact loading. Int J Impact Eng 2020;137:103432.

[32] Buth C.E., Williams W.F., Brackin M.S., Lord D., Geedipally S.R., Abu-Odeh A.Y. Analysis of large truck collisions with bridge piers: Phase 1, report of guidelines for designing bridge piers and abutments for vehicle collisions. No. FHWA/TX-10/ 9–4973-1. Texas: Texas Transportation Institute; 2010.

[33] Chen L, Xiao Y, El-Tawil S. Impact tests of model RC columns by an equivalent truck frame. J Struct Eng 2016;142:04016002.

[34] Zhou Y, Yang J, Luo X, Hwang HJ, Chen H, Sun J, et al. Pendulum impact loading tests of precast concrete columns with various column base connections. Eng Struct 2022;252:113736.

[35] Cotsovos DM, Stathopoulos ND, Zeris CA. Behavior of RC beams subjected to high rates of concentrated loading. J Struct Eng 2008;134:1839–51.

[36] Yi WJ, Zhao DB, Sashi KK. Simplified approach for assessing shear resistance of reinforced concrete beams under impact loads. Acids Struct J 2016;113:747–56.

[37] Liu T, Xiao Y. Impact behavior of CFRP-Strip–Wrapped RC beams without stirrups. J Compos Constr 2017;21:04017035.

[38] Hao H, Tran TT, Li H, Pham TM, Chen W. On the accuracy, reliability and controllability of impact tests of RC beams. Int J Impact Eng 2021;157:103979.

[39] Kishi N, Mikami H. Empirical formulas for designing reinforced concrete beams under impact loading. Acids Struct J 2012;109(4).

[40] Sun WB, Fan W, Yang CC, Peng WB. Lessons learned from vehicle collision accident of Dongguofenli Bridge: FE modeling and analysis. Eng Struct 2021;244:112813.

[41] Fan W, Xu X, Zhang Z, Shao X. Performance and sensitivity analysis of UHPFRC-strengthened bridge columns subjected to vehicle collisions. Eng Struct 2018;173:251–68.

[42] Fan W, Shen D, Zhang Z, Huang X, Shao X. A novel UHPFRC-based protective structure for bridge columns against vehicle collisions: experiment, simulation, and optimization. Eng Struct 2020;207:110247.

[43] Agrawal A.K., El-Tawil S., Cao R., Xu X., Chen X., Wong W. A performance-based approach for loading definition of heavy vehicle impact events. No. FHWA-HIF-18–062. Washington: U.S. Federal Highway Administration. Office of Research, Development, and Technology; 2018.

[44] LSTC. LS-DYNA Keyword user's manual. California: Livermore Software Technology Corporation; 2014.

[45] Xie RH, Fan W, Liu B, Shen DJ. Dynamic behavior and vulnerability analysis of bridge columns with different cross-sectional shapes under rockfall impacts. Structures 2020;26:471–86.

[46] Fan W, Shen D, Yang T, Shao X. Experimental and numerical study on low-velocity lateral impact behaviors of RC, UHPFRC and UHPFRC-strengthened columns. Eng Struct 2019;191:509–25.

[47] Fan W, Xu X, Zhang ZY, Shao XD. Performance and sensitivity analysis of UHPFRC-strengthened bridge columns subjected to vehicle collisions. Eng Struct 2018;173:251–68.

[48] Zhao DB, Yi WJ, Kunnath SK. Numerical simulation and shear resistance of reinforced concrete beams under impact. Eng Struct 2018;166:387–401.

[49] Adhikary SD, Li B, Fujikake K. Strength and behavior in shear of reinforced concrete deep beams under dynamic loading conditions. Nucl Eng Des 2013;259:14–28.

[50] Do TV, Pham TM, Hao H. Numerical investigation of the behavior of precast concrete segmental columns subjected to vehicle collision. Eng Struct 2018;156:375–93.

[51] Do TV, Pham TM, Hao H. Impact force profile and failure classification of reinforced concrete bridge columns against vehicle impact. Eng Struct 2019;183:443–58.

[52] Pham TM, Hao YF, Hao H. Sensitivity of impact behaviour of RC beams to contact stiffness. Int J Impact Eng 2018;112:155–64.